Faraday Discussions

Cite this: *Faraday Discuss.*, 2022, **236**, 141

PAPER

Evolution of surface and sub-surface morphology and chemical state of exsolved Ni nanoparticles†

Heath Kersell, *[a] Moritz L. Weber, [bc] Lorenz Falling,[a] Qiyang Lu,‡[a] Christoph Baeumer, [d] Nozomi Shirato,[e] Volker Rose,[ef] Christian Lenser, [c] Felix Gunkel [b] and Slavomír Nemšák *[a]

Received 18th December 2021, Accepted 4th March 2022
DOI: 10.1039/d1fd00123j

Nanoparticle formation by dopant exsolution (migration) from bulk host lattices is a promising approach to generate highly stable nanoparticles with tunable size, shape, and distribution. We investigated Ni dopant migration from strontium titanate (STO) lattices, forming metallic Ni nanoparticles at STO surfaces. *Ex situ* scanning probe measurements confirmed the presence of nanoparticles at the H_2 treated surface. *In situ* ambient pressure X-ray photoelectron spectroscopy (AP-XPS) revealed reduction from Ni^{2+} to Ni^0 as Ni dopants migrated to the surface during heating treatments in H_2. During Ni migration and reduction, the Sr and Ti chemical states were mostly unchanged, indicating the selective reduction of Ni during treatment. At the same time, we used *in situ* ambient pressure grazing incidence X-ray scattering (GIXS) to monitor the particle morphology. As Ni migrated to the surface, it nucleated and grew into compressed spheroidal nanoparticles partially embedded in the STO perovskite surface. These findings provide a detailed picture of the evolution of the nanoparticle surface and subsurface chemical state and morphology as the nanoparticles grow beyond the initial nucleation and growth stages.

[a]*Advanced Light Source, Lawrence Berkeley National Laboratory, Berkeley, California, 94720, USA. E-mail: hkersell@lbl.gov; snemsak@lbl.gov*

[b]*Peter Gruenberg Institute (PGI-7) and JARA-FIT, Forschungszentrum Jülich GmbH, 52425 Jülich, Germany*

[c]*Institute of Energy and Climate Research (IEK-1), Forschungszentrum Jülich GmbH, 52425 Jülich, Germany*

[d]*MESA+ Institute for Nanotechnology, University of Twente, Faculty of Science and Technology, 7500 AE Enschede, The Netherlands*

[e]*Center for Nanoscale Materials, Argonne National Laboratory, Lemont, Illinois, 60439, USA*

[f]*X-ray Science Division, Advanced Photon Source, Argonne National Laboratory, Lemont, Illinois, 60439, USA*

† Electronic supplementary information (ESI) available. See DOI: 10.1039/d1fd00123j

‡ Current address: Key Laboratory of 3D Micro/Nano Fabrication and Characterization of Zhejiang Province, School of Engineering, Westlake University, Hangzhou, Zhejiang, China.

1. Introduction

Nanoparticle catalysts supported on transition metal oxides play a critical role in chemical production and conversion, as well as energy conversion and storage processes.[1–4] Catalytic activity is affected by the nanoparticles' composition, size, structure, stability, and their interaction with the support. Decreasing the nanoparticle size increases the specific surface area and the density of low-coordination sites, often increasing activity. However, processes like nanoparticle coarsening, agglomeration, and coking can decrease activity through structural changes and decreases in available active sites.

In perovskite host lattices, catalytically active dopants can segregate to the oxide surface to form nanoparticles in a process known as 'exsolution'.[5] Recently, exsolution from perovskite hosts during reducing treatments produced metallic nanoparticles with excellent stability and coking resistance, as well as tunable size and distribution.[6–9] Particles exsolved from perovskite hosts exhibit strong metal–oxide interactions, producing nanoparticles partially embedded (socketed) in the oxide surface.[6,8,10] Surface enrichment by such exsolved metallic nanoparticles can enhance the electrocatalytic activity and surface conductivity of electrode materials.[11]

While the aforementioned properties of socketed nanoparticles are promising for a variety of applications, differences in perovskite host structure and composition, and differences in growth or reaction environments can lead to variations in particle size and shape.[12,13] Spherical, cubic, conical, and even core–shell particles have been observed, depending on the reaction environment.[10,13–15] Because particle shape can influence exposed active sites and activity, it is crucial to understand the evolution of the particle morphology during exsolution. To this end, recent investigations have probed the early stages of nanoparticle nucleation and growth to better understand the mechanisms leading to nanoparticle formation.[7,13] Because reaction environments influence the size, shape, and distribution of exsolved nanoparticles, it is crucial to understand their evolution during growth.

In this work, we monitor the chemistry and morphology of Ni nanoparticles as they migrate from $SrTi_{0.9}Nb_{0.05}Ni_{0.05}O_{3-\delta}$ (STNNi) hosts during reducing treatments in H_2 using a recently developed combination of ambient pressure X-ray photoelectron spectroscopy (AP-XPS), and ambient pressure grazing incidence X-ray scattering (AP-GIXS).[16] Ni reduces as it migrates to the surface, forming metallic nanoparticles partially embedded within the perovskite host lattice. Meanwhile, the oxidation state of the Sr and Ti in the host is mostly unchanged during the exsolution process. We used *ex situ* atomic force microscopy (AFM) and synchrotron X-ray scanning tunneling microscopy (SX-STM) to probe the *ex situ* surface structure and Ni distribution. Using this information to understand boundary conditions for the nanoparticle sizes and shapes, we used AP-GIXS to monitor the nanoparticle size and subsurface morphology during growth.

By combining AP-XPS and AP-GIXS in the same measurements, we reveal the evolution of chemistry and morphology during socketed nanoparticle growth by reduction in H_2 gas environments. Because both techniques possess tunable depth sensitivity, this approach is well suited to further studies of the chemistry and morphology of exsolved nanoparticles during exsolution and reactions, and

a host of other systems with dynamic structure and chemistry can also benefit from this approach.[17–19]

2. Methods

STNNi thin films of 30 unit cells (11.7 nm) were synthesized by reflection high-energy electron diffraction (RHEED)-controlled pulsed laser deposition (PLD) on (001) Nb-doped and TiO_2-terminated $SrTiO_3$ single-crystalline substrates (Shinkosha Co. Ltd., Yokohama, Japan). The thin films were deposited at $T = 650$ °C and at an oxygen pressure of $p(O_2) = 0.108$ mbar. A KrF excimer laser was applied for the ablation of the ceramic target material ($\lambda = 248$ nm) using a laser fluence of $F = 1.14$ J cm^{-2} and a repetition rate of $f = 5$ Hz. Here, two different PLD systems were used for the sample growth, which mainly differ in the respective heating systems. While an IR-diode laser ($\lambda = 925$ nm) is applied for heating in one of the systems (Surface GmbH), a resistive heater is applied for the other system (TSST – Twente Solid State Technology). In addition, slight differences in the target-to-substrate distance existed between systems, with $d = 57$ mm for the former and $d = 60$ mm for the latter PLD system. After the thin film growth, the samples were quenched to room temperature. Notably, the cooling rate was lower for the resistive heater, where the thermal history of the sample may cause small differences in the exsolution behavior.

The samples were 10 mm × 10 mm in size and were cut into 5 mm × 5 mm pieces after the thin film growth, which enabled the analysis of four nominally equal samples. For *ex situ* surface imaging, several samples were annealed under continuous 4% H_2/Ar gas flow ($t = 5$ h, $T = 800$ °C) in order to induce nickel exsolution. AFM was applied to investigate the surface morphology in the as-prepared state and after thermal reduction of the sample using tapping mode (AFM; Cypher, Oxford Instruments Asylum Research Inc., Santa Barbara, USA), with a tip curvature of approximately 8 nm. In order to obtain reference values for the nanoparticle dimensions, annealing experiments were carried out *ex situ* using one piece (5 × 5 mm) of four nominally equal samples that were cut from 10 × 10 mm^2 thin films that were used for the XTIP and AP-XPS/AP-GIXS investigations. The surface morphology was analyzed using the software package Gwyddion version 2.52, applying a lower threshold of 1 nm for the detection of the nanoparticles. The nanoparticle properties (nanoparticle density, median of the maximum nanoparticle height and the average nanoparticle diameter) were evaluated on the basis of a representative AFM scan with a size of 4 × 4 μm^2.

APXPS and APGIXS measurements were made on the sample spot, at the same conditions, in the same measurement set, using a recently developed ultrahigh vacuum system capable of simultaneous AP-XPS and AP-GIXS measurements. This system is located at undulator beamline 11.0.2.1 of the Advanced Light Source, which provides soft X-ray radiation between 160 and 1800 eV. The base pressure was 1×10^{-9} Torr at the start of the experiments, with water comprising most of the background gas. Photoelectron spectroscopy was conducted using a SPECS Phoibos ambient pressure hemispherical analyzer with 1D delay line electron detection. Binding energies (BEs) of core-level electrons were referenced using known BEs of Ti $2p_{3/2}$ (459.3 eV) and Sr 3d (134.2 eV) for the pristine STO and STNNi states.[20] The sample was mounted on a 4-axis manipulator, with three Cartesian translation axes supplemented by polar angle rotation (enabling

control of the X-ray incidence angle). Sample holders were equipped with a Pt button heater, permitting heating temperatures up to ~800 °C. To measure X-ray scattering from the STNNi surfaces, we used a CCD camera (Andor Ikon-L SO), which was isolated from the gas environment by an X-ray transparent 150 nm thick silicon nitride window (Silson Ltd.). Differential pumping was applied behind the X-ray window to maintain vacuum at the CCD chip surface and to prevent water condensation on the CCD chip, which was cooled to −50 °C during operation. The camera was mounted on a 2-axis universal mount, covering ±12° azimuthal and 20° polar scattering angles. More details on this setup can be found in ref. 16. A stainless steel beamstop was applied to block the reflected specular X-ray beam from saturating or even damaging the CCD camera. The beamstop appears as a vertical black rectangle along $\theta_f = 0°$ in all X-ray scattering data shown in this work, and additionally is the source of the circular feature near $\alpha_f = 0°$ in the experimentally obtained scattering patterns shown in the next section.

Analysis of grazing incidence X-ray scattering data requires the iterative simulation of X-scattering patterns emerging from various surface and near-surface geometries. BornAgain, a software package employing the distorted-wave Born approximation for simulating and fitting scattering at grazing incidence, was used to iteratively vary near-surface sample geometries and obtain agreement between the experimental and simulated scattering patterns.[21]

To probe the surface elemental composition of STNNi films after exposure to reducing treatments, we conducted X-ray absorption spectroscopy with an STM tip apex as the XAS detector at the XTIP beamline (4-ID-E) of the Advanced Photon Source.[22–24] The tip-sample junction of an STM was targeted with X-rays, and the X-ray absorption intensity was measured with the STM tip apex as a probe, with incident photons at 847 eV (before the Ni L_3-edge) and 852.2 eV (at the Ni L_3-edge) across a 216 nm × 300 nm region in 12 nm intervals. This approach provides the Ni XAS intensity at intervals smaller than the features expected on the STNNi surfaces discussed in the results. To prevent the detection of photoelectrons emitted from regions far from the tip apex, a coaxial "smart" tip was fabricated with a PtIr center, coated by layers of SiO_2, Ti, and Au.[23] To extract the X-ray induced contributions to the STM tunneling current, the incident X-ray beam was chopped at 650 Hz, and a phase sensitive filter extracted all beam-induced currents at the chopping frequency.[25] Throughout the course of the measurement, the sample was kept under 2×10^{-9} Torr and at room temperature. These measurements are presented in the ESI.†

3. Experimental results

3.1. *In situ* XPS of STNNi during reducing treatments

Fig. 1 shows the Ni 3p and Ti 3s photoemission spectra with 900 eV incident photons for an STNNi sample after progressive reducing treatments in 1 Torr H_2. In the as-prepared state, the Ni 3p feature above 68 eV is characteristic of Ni^{2+}.[7] Heating in 1 Torr of H_2 gas with increasingly higher temperatures and longer times shifts the position of the Ni 3p feature to 66.5 eV, characteristic of a transition to Ni^0. At the same time, the Ni 3p intensity increases notably compared to that of Ti 3s. This indicates that the surface becomes increasingly enriched in Ni^0 as the duration and temperature of the reducing treatments increase. This is in

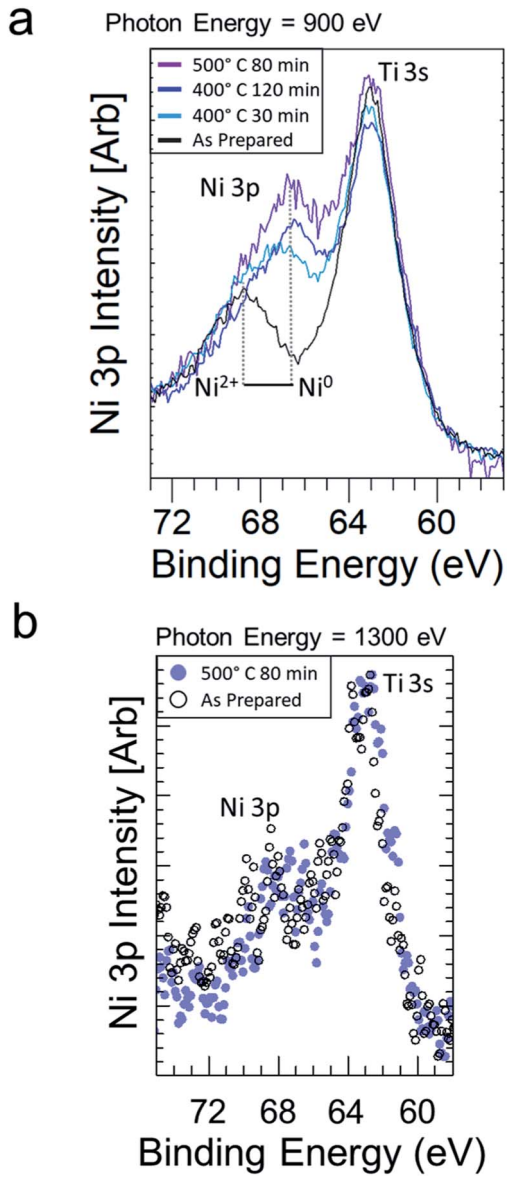

Fig. 1 (a) Ni 3p and Ti 3s regions at 900 eV photon energy are shown on STNNi after reducing in 1 Torr H_2 at increasing annealing times and temperatures. (b) Ni 3p and Ti 3s regions at 1300 eV photon energy measured on as prepared STNNi (black circles) and after annealing in 1 Torr H_2 at 500 °C. The increased photon energy in (b) is accompanied by a decrease in the photon flux, hence the results in (b) are displayed by dots rather than lines.

agreement with the tendency of Ni in STNNi to accumulate and form Ni-rich nanostructures fully embedded beneath the host surface, which then migrate to the surface to form nanoparticles upon reduction.[9]

To probe the sample composition deeper into the subsurface, we also measured the Ni 3p and Ti 3s regions with 1300 eV incident photons (Fig. 1b).

This increased the kinetic energy of the Ni 3p and Ti 3s electrons, thus increasing their inelastic mean free path (IMFP) from ~1.63 nm at 900 eV to ~2.23 nm at 1300 eV, and thus also increasing their probing depth.[26] In this greater depth, the Ni 3p area increased less than in the near-surface region probed in Fig. 1. Hence, while Ni migrates to the surface during reducing treatments, the sample composition was less affected in the sub-surface/bulk.

We also monitored the Sr and Ti composition and oxidation states during Ni reduction and migration. The Sr 3d and Ti 2p intensities both initially decrease (Fig. 2a and b), consistent with Ni enrichment at the STNNi surface. In spite of the reducing treatments and Ni migration, the Sr and Ti oxidation states remain mostly stable during the experiment. More quantitative discussion of the

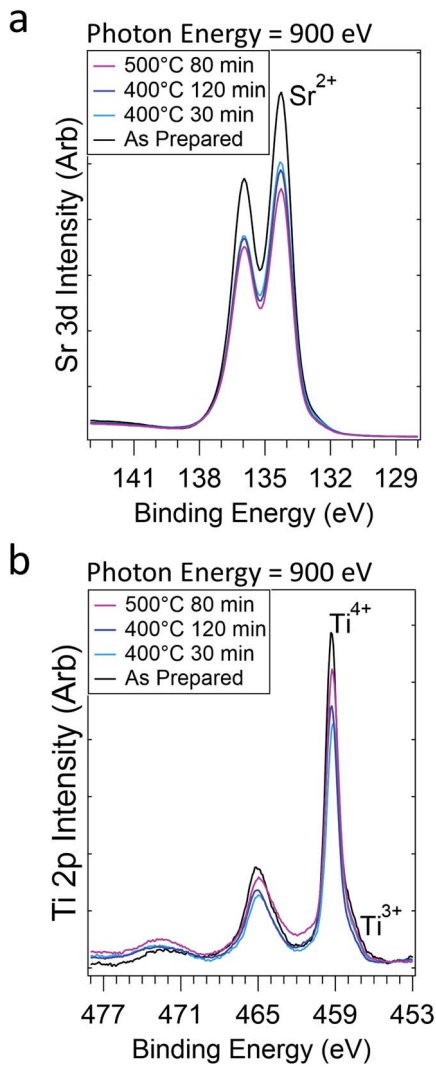

Fig. 2 Sr 3d (a) and Ti 2p (b) regions after increasingly reducing treatments in 1 Torr of H_2 gas. $E_{photon} = 900$ eV.

intensities is provided in the accompanying *Faraday Discussion*. Interestingly, previous investigations revealed the formation of Ni-rich nanostructures fully embedded beneath the STNNi surface.[9] The stability of the Sr and Ti oxidation states could suggest the migration of Ni from these nanostructures, leaving the perovskite structure otherwise intact. However, further investigation is necessary to confirm the subsurface sites from which the Ni migrates.

3.2. *Ex situ* AFM and elemental distribution

To understand the surface structure before and after Ni exsolution, we measured *ex situ* AFM on STNNi films in their as-prepared state, and after reducing at 800 °C for five hours in a 1 : 24 H_2 : Ar mixture. The as-prepared films exhibited a stepped-terrace structure (Fig. 3a) with 0.4 nm step height, equivalent to one $SrTiO_3$ unit cell.[27] After reducing in H_2, the surface was decorated with high contrast structures, averaging approximately 27.8 nm wide and 7.1 nm high (Fig. 3b). Lower contrast features were also present, with a height of 0.4 nm, consistent with the height of one $SrTiO_3$ unit cell (visible in Fig. 3b, inset). These lower contrast features possessed more varied geometries than the higher contrast features, had a typical width of 27.5 nm, and populated the surface more densely than the higher contrast features. The three-dimensional morphology of the brighter features is consistent with nanoparticle formation upon Ni exsolution,[9,12] while the 0.4 nm height of the low contrast features is consistent with the height of one $SrTiO_3$ unit cell. This suggests that the latter features are related to a relaxation or reconstruction of the STNNi host lattice during the reduction and nanoparticle formation. To further support the identification of the high contrast features as Ni nanoparticles, we also conducted X-ray absorption spectroscopy (XAS) using SX-STM to locally probe the surface composition of such a film already exposed to reducing treatment. The results are presented in the ESI,† and agree with the assignment of the high contrast features as exsolved Ni nanoparticles. The 0.4 nm height of the low contrast features observed in AFM suggests a possible

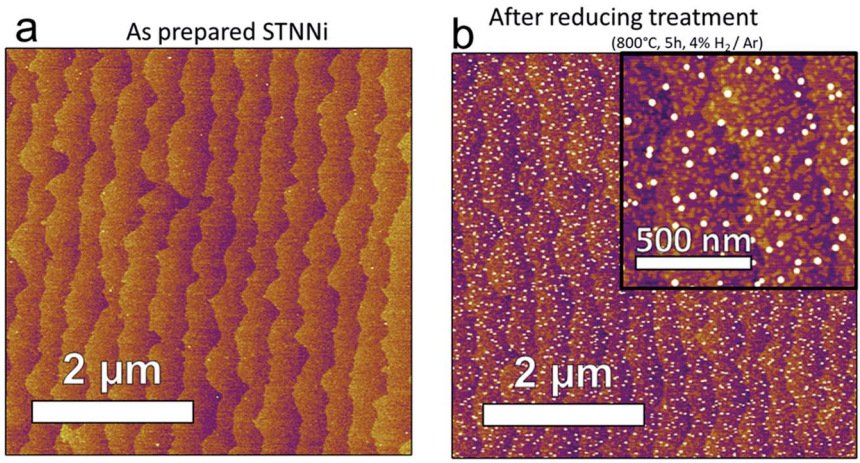

Fig. 3 *Ex situ* AFM imaging of STNNi surfaces in the as prepared state (a) and after reducing treatment in an H_2 : Ar mixture at 800 °C (b).

transformation of the STO host surface upon reduction and nanoparticle formation. Indeed, one potential explanation for the emergence of the lower contrast features is that Ni nanoparticle formation leaves behind subsurface Ni vacancies, generating structural instability in the host lattice.

3.3. GIXS of STNNi during reducing treatments

To understand the nucleation, growth, and evolution of Ni nanoparticles during reducing treatments, we collected GIXS from STNNi surfaces during the *in situ* XPS measurements shown in Fig. 1 and 2. This was done using a recently developed system enabling simultaneous *in situ* APXPS and APGIXS measurements on the same sample region.[16] The X-ray scattering geometry is shown in Fig. 4a, along with an illustration of its orientation with respect to the APXPS aperture of the hemispherical analyzer. This aperture provides a pathway for photoelectrons to travel from the sample to the electron energy analyzer, while limiting gas flow through the aperture.

X-ray scattering patterns (Fig. 4b–e) were collected during the measurements shown in Fig. 1 and 2 on probing regions overlapping with the XPS measurements, under the same conditions. This enabled the direct correlation between chemical, compositional, and structural transformations at each condition during *in situ* experiments. The sample that produced the scattering pattern in

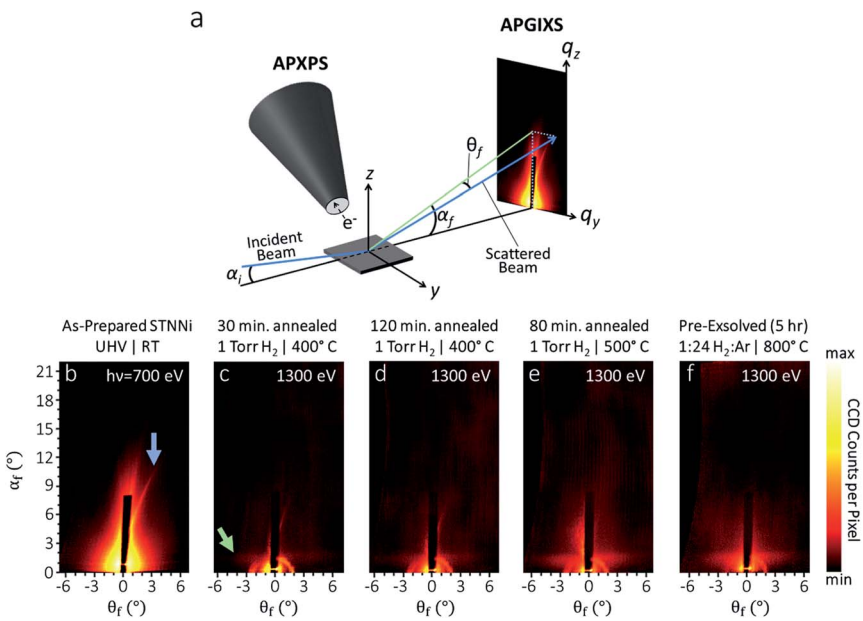

Fig. 4 (a) Combined AP-XPS-GIXS layout. Scattering patterns (b–f) measured from STNNi under progressively reducing conditions. (b) as prepared ('pristine'), (c) after annealing at 400 °C for 30 minutes in 1 Torr H_2 gas (green arrow shows the emergence of the Yoneda line), (d) annealed at 400 °C for 90 more minutes in 1 Torr H_2, (e) annealed at 500 °C for 80 more minutes in 1 Torr H_2, and (f) on an STNNi film pre-annealed *ex situ* at 800 °C in a 1 : 24 H_2 : Ar mixture for five hours and transferred through air to measure GIXS. [Scattering parameters: (a) $h\nu = 700$ eV, $\alpha_i = 1°$; (b–e) $h\nu = 1300$ eV, $\alpha_i = 0.4°$. Color bar is in logarithmic scale covering 4.3 orders of magnitude].

Fig. 4f was reduced *ex situ* by exposure to a 1 : 24 H_2 : Ar mixture at 800 °C for five hours prior to measurement, and was used as a limiting case for the *in situ* measurements. AFM on that sample revealed nanoparticles of 54 nm lateral width (not shown here). Hence, we limited the lateral size of the simulated particles to ~50 nm.

Before beginning the exsolution process by reducing in H_2, measurement of pristine STNNi targeted by 700 eV incident photons yields a clear scattering feature (indicated by an arrow in Fig. 4b) that is asymmetric with respect to the incident beam direction, appearing as a streak to one side of the beamstop. Asymmetric scattering with respect to the scattering plane (which is parallel to the incident beam direction and normal to the sample surface) requires scattering centers oriented asymmetrically with respect to the scattering plane. Faceted surface structures aligned off-axis from the scattering plane are one example of oriented features that can produce this behavior. In fact, our sample was mounted with the [100] crystal direction of the STNNi film rotated by approximately 10° azimuthally from the scattering plane, potentially explaining the presence of this asymmetric streak in the scattering. As we will discuss next, however, this feature is attributed to the STNNi step structure, which can have an orientation instead related to miscut directions during crystal fabrication.

In order to increase our capability to capture the form factor of smaller objects, subsequent measurements were done at a higher incident photon energy of 1300 eV. As a secondary effect, increasing the excitation energy also decreased the photon flux by almost an order of magnitude, slightly affecting the signal/noise ratio of following datasets. Further, at low angles, the polar scattering angle, α_f, varies inversely with the photon energy.[28]

After starting the exsolution process, when the STNNi was heated for increasing times and to higher temperatures in H_2, the asymmetric streak became more diffuse, and a new horizontally elongated diffuse feature emerged near $\alpha_f = 1.5°$ (Fig. 4c–f). This feature is related to the nucleation and growth of Ni nanoparticles partially embedded at the sample surface. We will next interpret these features within qualitative agreement with simulated scattering patterns.

3.4. Qualitative interpretation of Ni nanoparticles' morphology

X-ray scattering simulations were based on a model of partially embedded particles of varying size, shape, and nearest neighbor distance, together with linear/rectangular features mimicking terrace steps. Optimizing the geometry and distribution for each scattering pattern enables us to reveal trends in sample structure transformations emerging under each condition. To limit the simulation time, it is generally necessary to restrict simulations to a feasible set of sample geometries. Hence, based on information from *ex situ* AFM and SX-STM, we restricted the Ni particle geometries to spheres, compressed spheroids, hemiellipsoids, and hemispheres. These were allowed to have various distributions of diameters, heights, and nearest neighbor distances. The largest average particle sizes considered were 50 nm in diameter. The height of the nanoparticles above the STNNi film surface was limited to 8 nm.

Before reduction, the pristine STNNi surface produces an asymmetric streak with respect to the incident beam (blue arrow, Fig. 4b). This streak is consistent with a structure of a several hundred nanometer periodicity, oriented

asymmetrically with respect to the incident beam. The only sample feature fitting this description is the STNNi step structure. As such, we treated the STNNi steps by a periodic, partially disordered array of extremely elongated rectangular islands with 0.4 nm height, equal to the size of one $SrTiO_3$ unit cell (Fig. 5a).

Upon nanoparticle formation, the best qualitative agreement with the experiment was obtained for ellipsoidal particles embedded partially within the STNNi surface (Fig. 6a–f). For comparison, Fig. 6g–l show the result for spherical particles, partially embedded in the STNNi surface. In both cases, the average particle height above the surface was restricted to $\leq$8 nm. At 8 nm diameter, the spheres and the spheroids both produce a diffuse scattering feature near $\alpha_f = 1.5^\circ$, in agreement with the experiment. We note that $\alpha_f = 1.5^\circ$ is in the proximity of the critical angle for STNNi at 1300 eV, which explains the enhanced scattering intensity, otherwise known as the Yoneda line, at this region. The feature is relatively broad, since the exsolved nanoparticles cause increased film roughness compared to the initial atomically flat surface.

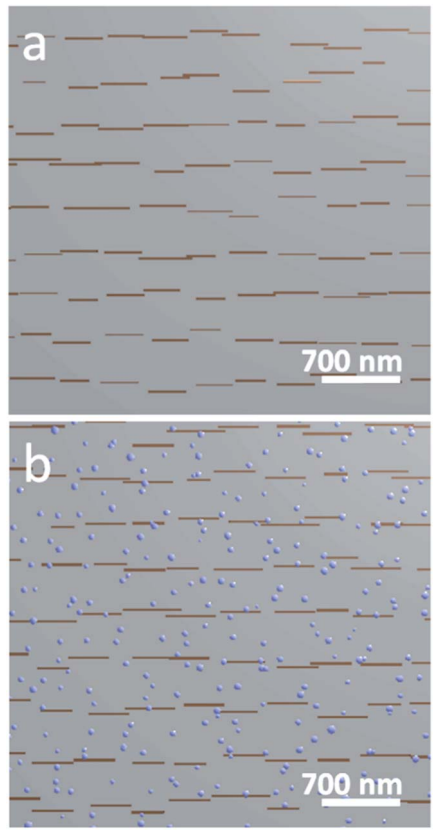

Fig. 5 (a) The pristine samples were modeled as flat STNNi surfaces with a partially ordered square lattice of rectangular islands having 20 nm width, 350 $\pm$ 75 nm length, and 400 $\pm$ 45 nm lattice periodicity, to simulate a disordered step geometry. (b) Surfaces containing exsolved Ni nanoparticles were treated by the inclusion of a disordered lattice of Ni particles whose size distribution and periodicity were increased with conditions to model the experimental particle geometries and distributions.

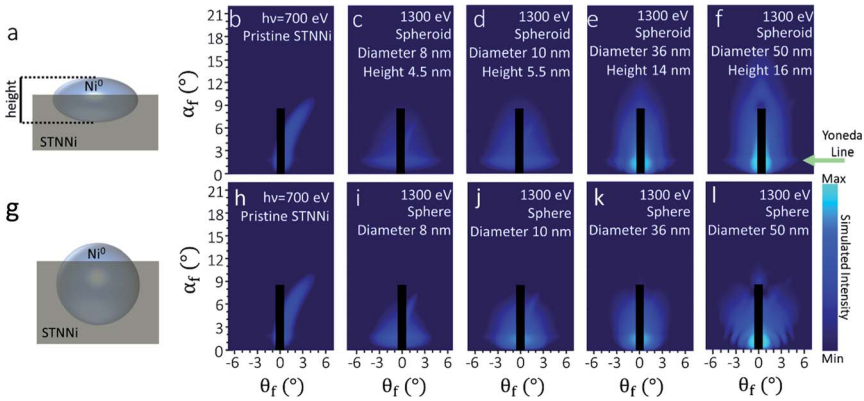

Fig. 6 Simulated scattering patterns for partially embedded spheroidal (a–f) and spherical (g–l) particles: the [100] surface direction of STNNi is rotated 11° azimuthally from the scattering plane. Each sequence begins with scattering from a pristine STNNi surface before nanoparticle formation (b and h), and is followed by scattering patterns from surfaces populated by Ni^0 nanoparticles of increasing diameter and height (b–f and h–l). The color bar is in $\log_{10}$, with arbitrary units crossing 5.5 orders of magnitude.

As the particle diameter increased to 50 nm, the spherical particles produced patterns deviating significantly from the experiment (Fig. 6k and l), with a compression of the Yoneda line and the development of a strong modulation in the form factor along q_y (*i.e.* along θ_f), which are not observed in the experiment. Meanwhile, spheroidal particles produced reasonable agreement across the entire range of particle sizes considered, with q_y modulations absent in the simulations due much lower nanoparticle heights.

The finding that exsolved Ni^0 nanoparticles adopt a significantly compressed spheroidal morphology is somewhat in contrast with previous investigations on smaller exsolved particles, which often appear more symmetric.[8,13] However, differences in the sample growth and exsolution environment significantly affect particle shape.[10,13–15] For example, the STNNi films measured in our experiments are only 12 nm thick, potentially limiting the nanoparticle height, while their lateral size is unrestricted. Moreover, Neagu *et al.* demonstrated the dependence of Ni nanoparticle shape on the concentration of Ni atoms in the perovskite host lattice.[13] It is also possible that a competition between surface and interfacial energies between the vacuum, Ni^0, and the STNNi host also favors the growth of increasingly compressed particles.

3.5. Ni nanoparticle formation quantified from XPS and GIXS experiments

Finally, to understand the correlation between Ni segregation and nanoparticle formation, we quantified both the metallic Ni intensity from the Ni 3p XPS region, and the integrated intensity of the Yoneda line feature, both at progressive stages of the exsolution process. It has been previously established that the Yoneda intensity can be used to assess roughness/inhomogeneities in planar systems, similar to the STNNi films presented here.[29]

The XPS intensity ratio between Ni^0 3p and Ti 3s is plotted in Fig. 7a, and the integrated Yoneda intensities are plotted in Fig. 7b. Ni 3p and Ti 3s intensities

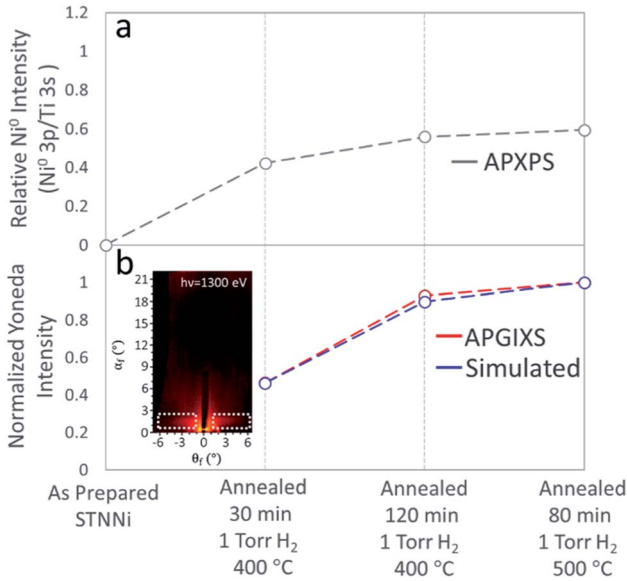

Fig. 7 (a) Relative Ni enrichment determined from Ni 3p intensity at the STNNi surface as a function of the reducing treatment. (b) Experimental (red) and simulated (blue) Yoneda line intensity as a function of treatment. The location of the Yoneda line is indicated by the dotted boxes in the inset scattering pattern. The intensity of the last point in (b) is normalized to 1 for both the APGIXS and simulated scattering patterns.

were determined by fitting the Ni 3p (two Voigt doublets, corresponding to Ni^{2+} and Ni^0) and Ti 3s (single Voigt spectral peak) regions (ESI†). Yoneda intensities were integrated in both the experimental and simulated scattering patterns across the region, illustrated by the inset in Fig. 7b.

No metallic Ni appears in the Ni 3p region of the as-prepared sample. Three further Ni 3p measurements upon annealing in H_2 show the increased intensity of the Ni^0 doublet (Fig. 1a and ESI†). The Ni^0 : Ti ratio first increases to ~0.42, and gradually evolves to ~0.59 (Fig. 7a). The Ni^0 XPS intensity increases by a factor of 1.4 between the first annealing condition (annealed for 30 min at 400 °C in H_2) and the last step of exsolution (80 min at 500 °C in H_2). The ratio of the Ni^0 3p to Ti 3s intensities for each condition was used, along with the experimentally obtained scattering patterns, to determine the particle sizes used in the simulations shown in Fig. 6.

The qualitative agreement between the increasing trends in the Ni^0 XPS signal and Yoneda line intensity confirms the increasing amount and size of the Ni nanoparticles. However, the Yoneda line intensity increases by a factor of ~2 between the first and the last step in the exsolution process. The explanation for these different amounts of signal enhancement (~1.4 in Ni^0 XPS and ~2 in the X-ray scattering Yoneda feature) can be found in the different quantities that XPS and X-ray scattering measure.

Even at a very grazing incidence, the information depth in soft X-ray photoelectron spectroscopy is still limited by the photoelectron inelastic mean free path (IMFP), or more precisely by the electron attenuation length. For the excitation energies used here, the photoelectron IMFP in STO is less than 2 nm, significantly

less than either the thickness of the STNNi film or the expected height of the exsolved nanoparticles. On the other hand, the penetration depth of X-rays and the evanescent wave associated with the incident X-ray wave cover the entire thickness of the STNNi film and penetrate through the nanoparticles in their entirety. As a direct consequence of the information depth difference, the XPS signal detecting Ni^0 atoms can only account for the topmost part (*ca.* 2–4 nm) of the nanoparticles, while the X-ray scattering signal originates from the scatterers throughout their entire volume.

For a fully quantitative comparison, corresponding photoelectron spectra (Ti 3s and Ni 3p) were simulated using the SESSA package[30] at each stage of the exsolution. The size and density of nanoparticles in the SESSA models were optimized to yield the same Ni^0 : Ti ratio in the simulated and experimental data. In a self-consistent manner, the same modeled size/density of nanoparticles were then iteratively used to generate scattering simulations in the BornAgain package (Fig. 6b–f). This structural and chemical model of the nanoparticles yields an excellent agreement for both spectroscopic and scattering data in Fig. 7a and b.

Both the Ni^0 XPS and Yoneda line intensities increase less between the last two conditions (120 min at 400 °C and 80 min at 500 °C). It is likely that the exsolution process began depleting the bulk of the STTNi film of nickel, and the nanoparticles' volumes continued slowly increasing. Within the accuracy explained above, the quantitative agreement between the increase in the Ni^0 XPS signal and the Yoneda line intensity also confirm the correlation between the morphology of the exsolved nanoparticles (elongated spheroid like particles) and their chemistry being metallic Ni. This observation of the exsolution process by both X-ray photoelectron spectroscopy and X-ray scattering provides a strong link between morphology and chemistry in the Ni nanoparticle/STNNi system.

4. Conclusions

Using *in situ* APXPS, we found that Ni migrated to the STNNi surface during reductive annealing treatments in 1 Torr of H_2 gas. Ni^{2+} was reduced to Ni^0 upon migration to the surface, while the Sr and Ti oxidation states were mostly unchanged. Increasing the XPS probing depth by increasing the photon energy revealed a less dramatic increase in Ni concentration, suggesting that the near-surface is less Ni enriched than the surface. *Ex situ* scanning probe measurements revealed approximately spherical Ni surface morphologies grown in response to reducing treatments. Throughout the nanoparticle growth process, *in situ* GIXS revealed the formation of spheroidal nanoparticles with a compressed geometry (Fig. 6a).

Because reaction environments influence the size, shape, distribution, and oxidation state of exsolved nanoparticles, it is crucial to understand their structural and chemical evolution *in situ* and under reaction conditions. Previous investigations have provided valuable insights into the atomic scale nucleation and early-stage growth of exsolved nanoparticles. To achieve atomic scale resolution, however, it is often necessary to use methods such as environmental transmission electron microscopy, which place stringent constraints on the sample geometry, such as the use of oriented, electron transparent samples. Here, we were able to simultaneously probe the dynamic Ni atom migration, chemical state evolution, and nanoparticle growth and morphology as the particles grew

beyond the initial stages of nucleation and growth, across the region illuminated by incident X-rays, hundreds of microns in width. The X-ray methods used here provide both surface and sub-surface information, which makes them perfect complementary techniques to scanning probes, such as STM or AFM.

Because exsolved nanoparticles were previously shown to have enhanced stability and coking resistance, these findings provide a detailed picture of the behavior of an important emerging class of catalysts. Additionally, this study serves as a proof of concept for monitoring *in situ* structural and chemical evolution in ambient gas and reaction environments by combining APXPS and APGIXS. For example, these methods can also be applied to directly correlate catalyst restructuring and chemical state evolution during reactions. Long standing questions of structure–activity relationships for many catalysts remain unanswered due to challenges in measuring the structure and chemical state of the catalyst *in operando*. Combining X-ray spectroscopies, scattering, and mass spectrometry/gas chromatography opens up possibilities to study how these transformations result from, and at the same time often drive, chemical activity.

Conflicts of interest

There are no conflicts of interest to declare.

Acknowledgements

This work was associated with the development of instrumentation through the Laboratory Directed Research and Development (LDRD) Program at Lawrence Berkeley National Laboratory under a grant titled "Correlation of structural and chemical processes at interfaces under operating conditions using multimodal ambient pressure X-ray photoelectron spectroscopy and surface X-ray scattering." S. N. and H. K. acknowledge this LDRD grant for salary support. Part of this work was performed at beamline 11.0.2 of the Advanced Light Source, a U.S. DOE Office of Science User Facility, which is funded under Contract No. DE-AC02-05CH11231. LJF acknowledges support from the Alexander von Humboldt Foundation, Bonn, Germany. Part of this work was performed at the Advanced Photon Source and the Center for Nanoscale Materials, U. S. Department of Energy Office of Science User Facilities, and supported by the U. S. Department of Energy, Office of Science, under Contract No. DE-AC02-06CH11357. The authors thank D. Rosenmann and Y. Liu for their help with smart tip fabrication at XTIP.

References

1 T. Mallat and A. Baiker, Oxidation of Alcohols with Molecular Oxygen on Solid Catalysts, *Chem. Rev.*, 2004, **104**, 3037–3058.
2 Q. Zhang, E. Uchaker, S. L. Candelaria and G. Cao, Nanomaterials for energy conversion and storage, *Chem. Soc. Rev.*, 2013, **42**, 3127.
3 A. S. Aricò, P. Bruce, B. Scrosati, J.-M. Tarascon and W. van Schalkwijk, Nanostructured materials for advanced energy conversion and storage devices, *Nat. Mater.*, 2005, **4**, 366–377.

4 Y. Nishihata, J. Mizuki, T. Akao, H. Tanaka, M. Uenishi, M. Kimura, T. Okamoto and N. Hamada, Self-regeneration of a Pd-perovskite catalyst for automotive emissions control, *Nature*, 2002, **418**, 164–167.
5 J. H. Kim, J. K. Kim, J. Liu, A. Curcio, J.-S. Jang, I.-D. Kim, F. Ciucci and W. Jung, Nanoparticle Ex-solution for Supported Catalysts: Materials Design, Mechanism and Future Perspectives, *ACS Nano*, 2021, **15**, 81–110.
6 D. Neagu, G. Tsekouras, D. N. Miller, H. Ménard and T. S. Irvine, *In situ* growth of nanoparticles through control of non-stoichiometry, *Nat. Chem.*, 2013, **5**, 916–923.
7 H. Han, J. Park, S. Y. Nam, K. J. Kim, G. M. Choi, S. S. P. Parkin, H. M. Jang and J. T. S. Irvine, Lattice strain-enhanced exsolution of nanoparticles in thin films, *Nat. Commun.*, 2019, **10**, 1471.
8 D. Neagu, T.-S. Oh, D. N. Miller, H. Ménard, S. M. Bukhari, S. R. Gamble, R. J. Gorte, J. M. Vohs and J. T. S. Irvine, Nano-socketed nickel particles with enhanced coking resistance grown in situ by redox exolution, *Nat. Commun.*, 2015, **6**, 8120.
9 M. L. Weber, M. Wilhelm, L. Jin, R. Dittmann, R. Waser, O. Guillon, C. Lenser and F. Gunkel, Exsolution of Embedded Nanoparticles in Defect Engineered Perovskite Layers, *ACS Nano*, 2021, **15**(3), 4546–4560.
10 D. Neagu, E. I. Papaioannou, W. K. Ramli, D. N. Miller, B. J. Murdoch, H. Ménard, A. Umar, A. J. Barlow, P. J. Cumpson, J. T. Irvine and I. S. Metcalfe, Demonstration of chemistry at a point through restructuring and catalytic activation at anchored nanoparticles, *Nat. Commun.*, 2017, **8**, 1855.
11 Y. Li, W. Zhang, Y. Zheng, J. Chen, B. Yu, Y. Chen and M. Liu, Controlling cation segregation in perovskite-based electrodes for high electro-catalytic activity and durability, *Chem. Soc. Rev.*, 2017, **46**, 6345.
12 K. J. Kim, H. Han, T. Defferriere, D. Yoon, S. Na, S. J. Kim, A. M. Dayaghi, J. Son, T.-S. Oh, H. M. Jang and G. M. Choi, Facet-Dependent *in Situ* Growth of Nanoparticles in Epitaxial Thin Films: The Role of Interfacial Energy, *J. Am. Chem. Soc.*, 2019, **141**, 7509–7517.
13 D. Neagu, V. Kyriakou, I. L. Roiban, M. Aouine, C. Tang, A. Caravaca, K. Kousi, I. Schreur-Piet, I. S. Metcalfe, P. Vernoux, M. C. M. van de Sanden and M. N. Tsampas, *In Situ* Observation of Nanoparticle Exsolution from Perovskite Oxides: From Atomic Scale Mechanistic Insight to Nanostructure Tailoring, *ACS Nano*, 2019, **13**(11), 12996–13005.
14 S. Liu, Q. Liu and J.-L. Luo, HighlyStable and Efficient Catalyst with *In Situ* Exsolved Fe-Ni Alloy Nanospheres Socketed on an Oxygen Deficient Perovskite for Direct CO_2 Electrolysis, *ACS Catal.*, 2016, **6**, 6219–6228.
15 W. K. W. Ramli, E. Papaioannou, D. Naegu and I. S. Metcalfe, Exsolution of nickel alloys anchored nanoparticles on perovskite oxides for CO oxidation, *IOP Conf. Ser.: Mater. Sci. Eng.*, 2020, **778**, 012059.
16 H. Kersell, P. Chen, H. Martins, Q. Lu, F. Brausse, B.-H. Liu, M. Blum, S. Roy, B. Rude, A. Kilcoyne, H. Bluhm and S. Nemsák, Simultaneous ambient pressure X-ray photoelectron spectroscopy and grazing incidence X-ray scattering in gas environments, *Rev. Sci. Instrum.*, 2021, **92**, 044102.
17 B. Eren, D. Zherebetskyy, L. L. Patera, C. H. Wu, H. Bluhm, C. Africh, L.-W. Wang, G. A. Somorjai and M. Salmeron, Activation of Cu(111) surface by decomposition into nanoclusters driven by CO adsorption, *Science*, 2016, **351**(6272), 475–478.

18 J. Wang, M. McEntee, W. Tang, M. Neurock, A. P. Baddorf, P. Maksymovych and J. T. Yates, Jr., Formation, Migration, and Reactivity of Au-CO Complexes on Gold Surfaces, *J. Am. Chem. Soc.*, 2016, **138**, 1518–1526.

19 T. W. Hansen, A. T. DeLaRiva, S. R. Challa and A. K. Datye, Sintering of Catalytic Nanoparticles: Particle Migration or Ostwald Ripening, *Acc. Chem. Res.*, 2013, **46**(8), 1720–1730.

20 S. Nemšák, G. Conti, A. X. Gray, G. K. Palsson, C. Conlon, D. Eiteneer, A. Keqi, A. Rattanachata, A. Y. Saw, A. Bostwick, L. Moreschini, E. Rotenberg, V. N. Strocov, M. Kobayashi, T. Schmitt, W. Stolte, S. Ueda, K. Kobayashi, A. Gloskovskii, W. Drube, C. A. Jackson, P. Moetakef, A. Janotti, L. Bjaalie, B. Himmetoglu, C. G. Van de Walle, S. Borek, J. Minar, J. Braun, H. Ebert, L. Plucinski, J. B. Kortright, C. M. Schneider, L. Balents, F. M. F. de Groot, S. Stemmer and C. S. Fadley, Energetic, spatial, and momentum character of the electronic structure at a buried interface: The two-dimensional electron gas between two metal oxides, *Phys. Rev. B*, 2016, **93**, 245103.

21 G. Pospelov, W. Van Herck, J. Burle, J. M. C. Loaiza, C. Durniak, J. M. Fisher, M. Ganeva, D. Yurov and J. Wuttke, BornAgain: software for simulating and fitting grazing-incidence small-angle scattering, *J. Appl. Crystallogr.*, 2020, **53**(1), 262–276.

22 H. Kersell, N. Shirato, M. Cummings, H. Chang, D. Miller, D. Rosenmann, S.-W. Hla and V. Rose, Detecting element specific electrons from a single cobalt nanocluster with synchrotron X-ray scanning tunneling microscopy, *Appl. Phys. Lett.*, 2017, **111**, 103102.

23 N. Shirato, M. Cummings, H. Kersell, Y. Li, B. Stripe, D. Rosenmann, S.-W. Hla and V. Rose, Elemental Fingerprinting of Materials with Sensitivity at the Atomic Limit, *Nano Lett.*, 2014, **14**(11), 6499–6504.

24 V. Rose, N. Shirato, M. Bartlein, A. Deriy, T. Ajayi, D. Rosenmann, S.-W. Hla, M. Fisher and R. Reininger, XTIP - the world's first beamline dedicated to the synchrotron X-ray scanning tunneling microscopy technique, *J. Synchrotron Radiat.*, 2020, **27**(3), 836–843.

25 K. Wang, D. Rosenmann, M. Holt, R. Winarski, S.-W. Hla and V. Rose, An easy-to-implement filter for separating photo-excited signals from topography in scanning tunneling microscopy, *Rev. Sci. Instrum.*, 2013, **84**, 063704.

26 C. J. Powell and A. Jablonski, *NIST Electron Inelastic-Mean-Free-Path Database*, National Institute of Standards and Technology, Gaithersburg, MD, 2010.

27 F. W. Lytle, X-Ray Diffractometry of Low-Temperature Phase Transformations in Strontium Titanate, *J. Appl. Phys.*, 1964, **35**, 2212.

28 P. Müller-Buschbaum, A Basic Introduction to Grazing Incidence Small-Angle X-ray Scattering, in *Applications of Synchrotron Light to Scattering and Diffraction in Materials and Life Sciences*, Springer, Heidelberg, 2009, pp. 61–89.

29 C. Frank, J. Novak, R. Banerjee, A. Gerlach, F. Schreiber, A. Vorobiev and S. Kowarik, Island size evolution and molecular diffusion during growth of organic thin films followed by time-resolved specular and off-specular scattering, *Phys. Rev. B: Condens. Matter Mater. Phys.*, 2014, **90**, 045410.

30 W. Smekal, W. S. M. Werner and C. J. Powell, Simulation of electron spectra for surface analysis (SESSA): a novel software tool for quantitative Auger-electron spectroscopy and X-ray photoelectron spectroscopy, *Surf. Interface Anal.*, 2005, **37**, 1059–1067.